Composites: Part A 188 (2025) 108562

Contents lists available at ScienceDirect

Composites Part A

journal homepage: www.elsevier.com/locate/compositesa

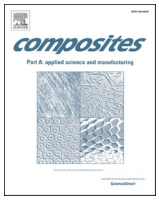

Combination of in-/and ex-situ damage detection methods to investigate the forming behavior of fiber-metal-laminates

Florian Thum, Marco Korkisch, Anna Trauth, Markus G.R. Sause *

University of Augsburg, Institute of Materials Resource Management, Am Technologiezentrum 8, 86159 Augsburg, Germany

ARTICLE INFO

Keywords:
Failure analysis
Fiber Metal Laminates
X-Ray Computed Tomography
Acoustic Emission Measurement
Digital Image Correlation

ABSTRACT

In this study, the forming behavior of fiber-metal laminates (FML) is investigated by a combination of different (in- and ex-situ) measurement techniques. Using FML-samples consisting of aluminum and carbon fiber reinforced polyamide-6, deep-drawing tests were employed at high temperatures. It can be concluded a conventional approach based on the forming limit curve (FLC) is not suitable to predict the failure initiated in the multi-material setup as principal strains cannot differentiate the strain in aluminum and CFRP and lack sensitivity to detect other relevant failure modes, such as debonding as well as debonding in between layers. To better understand the failure behavior due to forming of FML, an experimental setup, that based on the Nakajima-test, was developed, using in-situ acoustic emission testing, 3D digital image correlation as well as ex-situ X-ray computed tomography. The combined results from all methods helped to gain a deeper insight into how thermoplastic FML behave during deep drawing at elevated temperatures especially focusing on evolving damage inside the hybrid material.

1. Introduction

Fiber reinforced polymers (FRP) have the ability to outperform monolithic metals in many applications, especially considering their lightweight potential due to their high specific mechanical properties and corrosion resistance. Nevertheless, it is often not feasible to simply exchange existing metal structures with ones made from FRP. In many industry fields, like aviation, there are established manufacturing processes that have been investigated and refined for decades, that cannot simply be adapted for the use with FRPs. Also, the very specific failure characteristics of FRPs are not acceptable in some applications. Therefore, fiber metal laminates (FML), made from alternating layers of metal sheets and FRP, have been developed to create not only a compromise between these two material types, but also to emphasize the strength of both by canceling out many of their individual weaknesses. [1,2] After a long time, where FML where mainly used in very specific applications like airplane fuselages [3,4], one focus of today's research in FML is targeted towards more automated production and processing to decrease costs and therefore make it available to new fields of applications. One part of this research is the use of thermoplastic matrix polymers instead of the often used thermoset alternatives. The potential to manufacture semi-finished products and perform forming steps independently makes automating the process much easier. [5,6,7,8] Also, despite more focus on the forming temperature is required, the process of forming thermoplastic FML is closely related to sheet metal forming. Therefore, the investigations based on a adapted Nakajima-testing setup were carried out within this study. In the forming process, the aim is to achieve a high degree of forming combined with high strengths. The criteria for evaluating and classifying formed components vary widely as the geometries become more complex and the fields of application become more extensive. In addition to failure due to fractures, potential defects include local necking, wrinkling and surface defects. The development of these defects is caused by a wide range of factors. In addition to defects in the original raw material, damage of the forming tool and forming parameters can have an influence on the resulting component. Since material cohesion is lost in the case of a crack, this most obvious failure case is the most important criterion for evaluation in sheet metal forming. The methods for material characterization are manifold, and the description possibilities for materials grow with the requirements for material and component. Material behavior can be modeled and predicted by mathematical approaches. The desire for more accurate predictions and the use of more complex simulations continue to drive the requirements for material characterizations. Two input variables are required for sheet metal forming

* Corresponding author.
E-mail address: markus.sause@uni-a.de (M.G.R. Sause).

https://doi.org/10.1016/j.compositesa.2024.108562
Received 14 August 2024; Received in revised form 25 October 2024; Accepted 26 October 2024
Available online 5 November 2024

simulation. One is the yield locus curve, which describes the transition from elastic to plastic behavior of a material as a function of the stress state, and the other is the yield curve, which refers to the material hardening during continuous plastic deformation. In application, the von-Mises approach, which is based on the shape change-energy hypothesis, is usually used to inform the yield curves for isotropic materials. It assumes that plastic flow sets in when the elastic deformation energy per volume reaches a material-dependent threshold [9]. In order to describe a forming process more accurately, the yield locus curve must be scaled in the context of the hardening law. This is determined by the strain hardening information of the yield curve [10]. In finite element analysis (FEA), it can now be determined at which stresses the material plasticizes. The required forming forces can be determined at a stress generated by the forming process. With the aid of the forming limit curve, a failure analysis can be carried out in the next step. This describes which strains lead to failure as a function of the first and second principal deformation.[11]. The failure limit is considered at least at five different stress states to derive a complete understanding of failure induced by a forming process. In addition to the material selection, the following process parameters play an important role for forming [12,13]: the deep drawing speed, the tribological lubricant system, the punch geometry (Nakajima/Marciniak), strain state, strain rate and temperature. Important evaluation parameters are the image acquisition frequency of the optical measuring system, the fineness of the stochastic pattern and the evaluation method [14,15]. The material-related influencing factors include the material thickness, the surface quality and, in the case of multilayer material systems, the configuration of the material [16,17]. In a publication by Hiroi and Nishimura [18], the influence of surface defects on the behavior of the forming limit curve is discussed. The materials aluminum 1070-O and 1070-H26 were investigated at 0° and 90° to the rolling direction using several test methods. Artificial surface defects were introduced to determine the influence on the respective test method. When the forming limit curve was determined, it was found that the values for artificially introduced defects with depths up to 2 % of the thickness for soft annealed aluminum specimens (1070-O) and 0.5 % for the hard aluminum specimens had a negligible influence on the results. In a publication by Smith [19], the aluminum alloys 2010-T4 and 6111-T4 are tested with different plate thicknesses to investigate the influence on the forming limit curve. In his evaluations, Smith shows that in tests on aluminum, the thickness of the specimens has significantly less influence on the deformation than in the case of steel. The selected specimen thicknesses were between 0.5 mm and 2 mm. In the work of Tasan et al. [20], an in-situ miniature setup for Marciniak experiments in the scanning electron microscope (SEM) is presented, which merges damage mechanisms on a microscopic level with macroscopic failure. Among other materials, the 6061-aluminum alloy is examined. With the help of the SEM images, the inclusions in the aluminum alloy could be assigned as the cause of the initial damage. Due to the different forming properties at elevated temperatures of metals, the process temperature also plays an important role in the investigation of the forming limit curve for FML. The forming capacity of metals can be increased by raising the temperature [21]. The mechanisms for this are, on the one hand, the healing of one-dimensional defects, which means the annihilation of two opposite step or screw dislocations. On the other hand, a rearrangement of zero-dimensional defects occurs, which describes the insertion of vacancies and interstitial atoms into lattice half-planes of dislocations. These thermal recovery processes lead to material recovery and eventually to an extension of the deformation capacity [22]. The temperature effect on the forming limit behavior in metals has already been studied in various works [10,23,24]. In a study by Hsu et al. [25], magnesium alloys are tested using Nakajima and Marciniak tests at 300 °C. It was found that, especially for tests at elevated temperatures, care must be taken to use suitable lubrication systems, since common agents are not sufficiently stable at elevated temperatures. In Hsu's work, graphite- and boron nitride-based lubrication systems are therefore used. Nevertheless, a fully valid evaluation could not be made due to offcenter failure of the samples. In addition to a suitable lubrication system at elevated temperatures, attention must be paid to uniform heating of the forming tool, which is evident in the work of Dahan et al. [26]. Here, the specimens are heated outside the tool. Inside the test fixture, rapid cooling of the specimen occurs upon contact with the die. The optical measurement system confirms an off-center strain distribution. In the work of Bariani et al. [27] and Turetta [28], the stamp of the set-up is additionally heated with heating cartridges. The temperature distribution is checked by using several thermocouples and measurement by thermocamera. Both measurements still show a temperature gradient from the cooler specimen center with stamp contact towards the edges. However, this could be reduced and valid specimens with central failure could be produced. A summary on the influence of the test conditions can be found in the work of Kuppert [10] and Merklein et al. [29]. As shown by literature the Nakajima-test is a well established method to identify the forming behavior of metallic materials depending on various material properties and process parameters. In addition, various attempts have been made to facilitate measurement of deformation by digital image correlation for example. However, this method might only be applied in its original sense to this type of monolithic materials (metals) and does not lead to meaningful results if hybrid materials are considered. This is due to the complex failure behavior and mostly superposing failure mechanisms as well as a failure evolution that is not primarily driven by plastic deformation. With this starting point main research questions of this publication is to find out if different in- and ex-situ measurement systems can be combined in a way that data that is either resolved in time, space or both can be captured in a heated environment with no direct access to the specimen and furthermore, synchronized afterwards to provide insight on evolving failure, especially resulting due to the complex structure of hybrid materials. In detail, this work in particular aims to answer the questions if a combination of digital image correlation, acoustic emission and computed-tomography enable to investigate failure behavior of fiber-metal laminates that are loaded perpendicular by a punch (Nakajima test) to understand limits of formability. Hence, this work provides the basis for the experimental investigation of forming behavior of fiber-metal laminates based on multiple in-/and ex-situ measurement techniques for failure investigations. This approach enables not only to consider plastic deformation and strain evolution but also to localize damage and distinguish between different failure mechanisms. In detail, the testing of FML materials is accompanied by digital image correlation and acoustic emission as well as X-ray computed tomography in order to provide a comprehensive understanding of the failure mechanisms and failure evolution resulting from forming of fiber-metal-laminates.

2. Material preparation and experimental setup

2.1. Tested materials

For the CFRP laminates a prepreg from the company SGL Carbon GmbH was considered. The semi-finished products with polyamide-6 matrix contain high-tensile (HT) C-fibers, which are sold under the commercial name Sigrafil® (Sigrafil C T50-4.0/240-T140). For the metal layers, aluminum foil EN AW – Al 1050A (Alujet GmbH) with a thickness of 0.3 mm and a tensile strength of 95 MPa was used [30]. The selection of materials was based on the materials commonly used in forming technology. For the series of tests on FML, test specimens with the configuration Al – $[0°_2, 90°_2, 0°_2, 90°_2]_{sym}$ – Al were cut out of plates using a water jet cutter. The plates were produced by hot pressing and the thickness was 4.1 mm. Fig. 1a shows an FML-Nakajima specimen with a blank width S_B of 30 mm. Fig. 1b shows the geometry of the specimens required by the corresponding standard [31] for determining the deformation.

For the tests, the parameters $R_I = 30$ mm, $R_A = 80$ mm, $S_H = 35$ mm and blank widths of $S_B = 30$ mm, 50 mm, 70 mm, 90 mm as well as a full

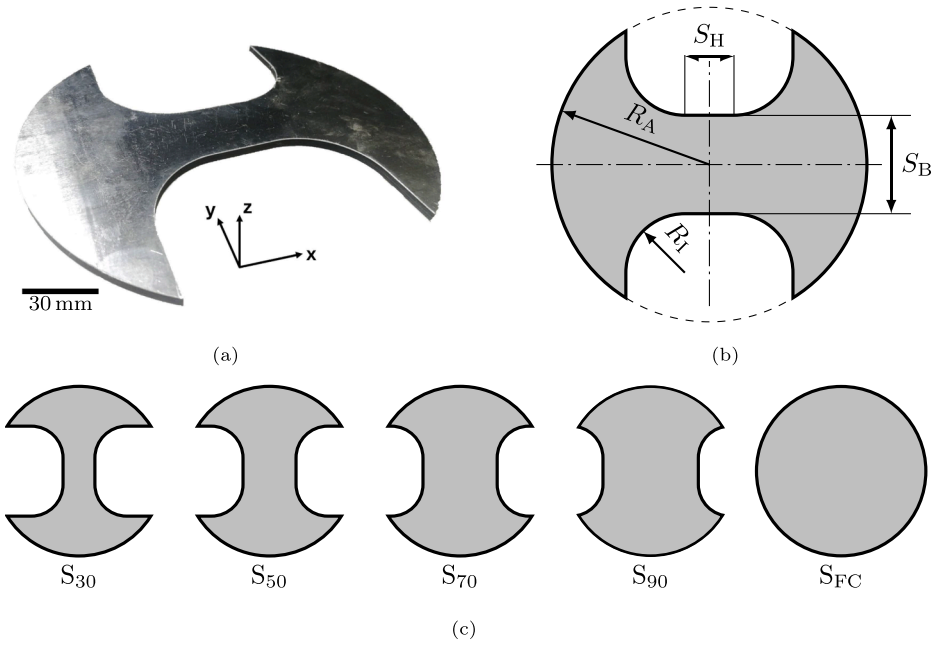

Fig. 1. Image of a hybrid sample with a blank width S_B of 30 mm (a), a schematic of the specimen dimensions with variable blank width S_B up to a full circle shape indicated with a dashed line (b) and sketches of all five used sample geometries (c).

circle were selected. As load is applied using a halfspherical punch, which moves onto the sample in its thickness-direction, load on a full circle will result in a uniform deformation, while a small blank width of $S_B = 30$ mm leads to an approximately uniaxial load in the *x*-direction of the sample. In total only one sample of each of the five geometries was tested with step-increments to perform the X-ray scans (see section 3.3), as the study was focused on the methodology, not the determination of material properties. They are named S_{30}, S_{50}, S_{70}, S_{90} and S_{FC} according to their blank width S_B up to the full circle geometry.

2.2. Experimental setup

In order to investigate the deep drawing properties of aluminum and the newly developed FML, a test rig for Nakajima tests at temperatures up to 250 °C was newly developed (Fig. 2). For the geometry of the dies and specimens, DIN EN ISO 12004–2 [11] was considered. The baseplate and die as parts of the sample holder have an outer diameter of 190 mm and an opening with a diameter of 110 mm. In addition, both have a roughened inner surface to prevent the specimen from being pulled out. In addition, the die has a radius of 10 mm at the inner edge to prevent shearing of the specimen. The specimen is clamped by bolting the plates together with four M8 bolts. The 50 kN testing machine (Kappa DS, Zwick/Roell) moves the die with a crosshead controlled by a stepper motor. The setup is designed and tested for forces up to 70 kN and can thus be loaded up to the maximum load capacity (50 kN) of the testing machine. In order to achieve the desired temperature and to enable uniform heating of the buildup, four additional heating cartridges with a total heating power of 280 W are integrated into the die (see Fig. 2). The

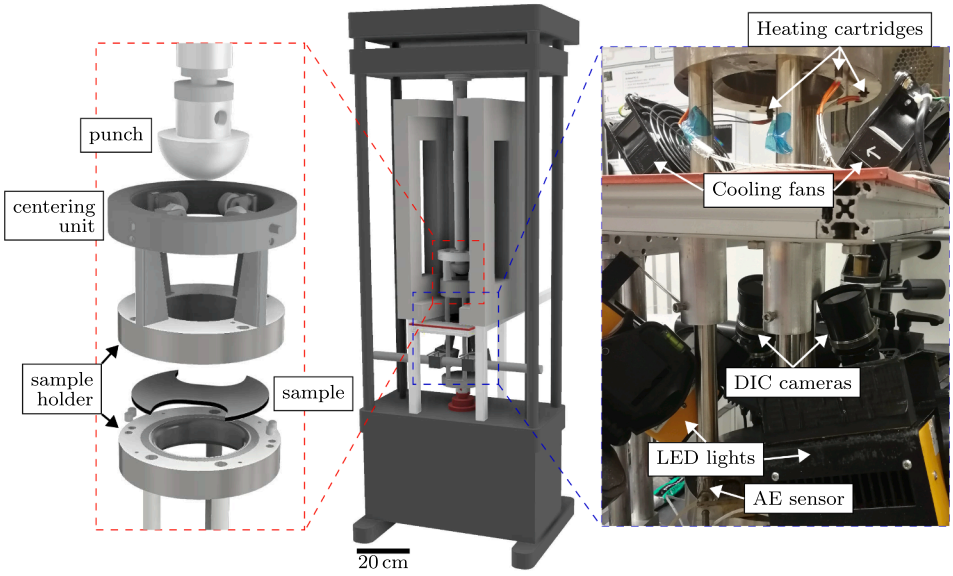

Fig. 2. Front view of the CAD model of the developed Nakajima setup in a universal testing machine with detailed views of the sample holder (left) and an image of the setup with sensors, as well as heating and cooling equipment (right).

convection oven can be controlled to a maximum temperature of 250 °C. Due to the heat dissipation of the tools connected to the outside, the heating cartridges must be controlled to 270 °C in order to heat the clamped specimens to 240 °C. The control of the heating cartridges takes place at the thermocouple between baseplate and die. The temperature curve in the specimen is recorded in parallel during the test. Care was taken to use a sufficiently thin thermocouple to minimize the influence of pressing on the specimen. This was applied to the edge of the specimen outside the relevant test area. To monitor the deformation of the tested specimens during deep drawing the 3D digital image correlation system ARAMIS 4 M by GOM was used. The two cameras and LED lights were installed below the temperature chamber to ensure a full view on the whole specimen from the bottom. The system was setup in a way to allow big enough measurement volume, which is necessary to monitor the high displacement values up to 70 mm in the middle of the samples. In order to quantify the amount of failure in the form of cracks and delamination, introduced during cooling of the samples, acoustic emission analysis was also implemented in the test setup. For that purpose, three acoustic emission sensors (WD-sensors from Physical Acoustics) were placed at the lower end of the struts connecting the sample holder and the force cell at the bot-tom. This position was chosen as the maximum temperature rating for these type of sensors as provided by the manufacturer is 177 °C and placement on the samples themselves was not feasible due to their ongoing deformation. The struts act as a waveguide system that allows the signals to travel from the actual sample to the sensor position, a commonly used concept when sensors cannot be exposed to elevated test temperatures [32]. Using 2/4/6-pre-amplifiers also by Physical Acoustics and an acquisition system, acoustic emission signals were recorded during the forming and cooling process. For recording, a detection threshold of 40 dB, preamplification of 40 dB, a high pass filter at 1 kHz and a low pass filter at 3 MHz were used.

2.3. Experimental procedure

In contrast to the standard test procedure of the Nakajima test, where the deep drawing is performed in one step until failure, in this case the forming of the specimens was conducted in several steps of 5 mm of crosshead displacement. During these steps of the forming process (shown in Fig. 3) the samples.

were monitored using data from the testing machine, digital image correlation, acoustic emission and the thermocouples. Between the steps CT scans were performed to investigate the internal structure of the samples. Therefore, each step consists of mounting the sample, heating it above the melting temperature of the matrix material, additional clamping of the sample, deep drawing it for additional 5 mm, cooling it down, unmounting it and performing the CT scan. These steps were repeated until the outer aluminum layer showed visible failure in the form of cracks.

3. Data evaluation

3.1. Digital image correlation

The full field deformation data obtained by digital image correlation allow quantitative evaluation of the load condition as common for the Nakajima test, as well as qualitatively investigating abnormalities visible in the evaluated deformation data. The data were evaluated using GOM Correlate Professional, where all relevant deformation properties were investigated. For the quantita-tive load condition, mean values of major and minor strain were evaluated in a circular region of interest with a diameter of 20 mm in the center of all samples. Therefore, for every step of forming for every sample, the development of the load condition in form of the ration of major and minor strain can be obtained. As the forming was conducted in steps and every measurement with DIC is referenced to its starting condition, the curves for every step were added up to result in a cumulative curve. In contrast to the classical evaluation, where major and minor strain are evaluated only right before failure, this allows to investigate the entire development of the load condition as seen by the outer metal layer of the FML. On the one hand, this procedure enables to compare the load condition of a FML specimen to monolithic metallic samples, but on the other hand to also detect deviations from an expected load condition.

3.2. Acoustic emission measurement

Acoustic emission analysis was integrated to obtain information on occurring defects during the cool down phase after the forming step. Using the software nAExtor by BCMtec GmbH, a feature extraction was performed on all detected acoustic signals, resulting in more detailed information about failure. For monitoring, three individual sensors were used, to enable a localization of the detected signals [15]. Due to the distance between the sensors and the sample and the complex structure of the tooling used, a accurate localization within the sample itself was not possible. But the time difference between the same signal reaching the three sensors, enabled filtering for signals, which originated from the region of the sample. This was performed using a Δt-Filter of 100 µs between all three channels.

3.3. X-ray computed tomography

Due to the volumetric data sets generated during CT analysis, defects can be precisely analyzed based on the gray value differences within the examined materials with suitable image quality. In order to be able to resolve a certain target pore size, a voxel size must be chosen that is

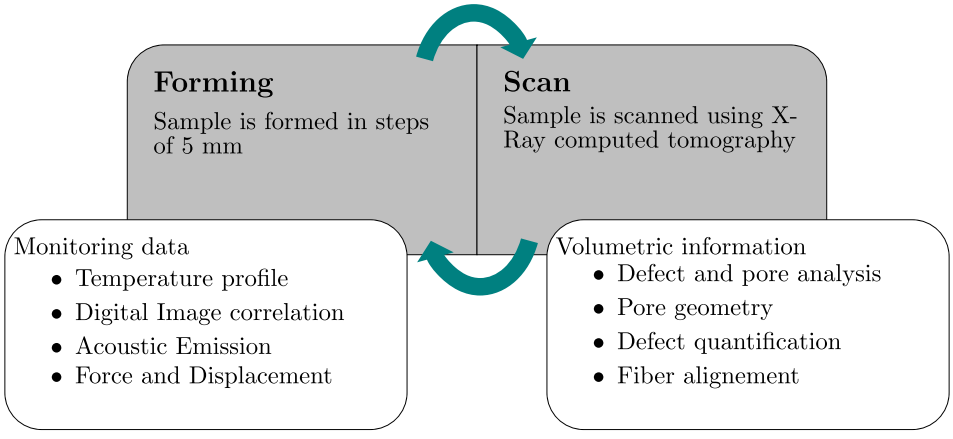

Fig. 3. Schematic of the combined in- and ex-situ approach for the Nakajima testing of hybrid specimens.

approximately three times smaller than the object to be detected [33]. However, for a more accurate description of the geometric attributes of a segmented defect, an even finer resolution is desirable. A distinction between larger voids (defects) and (micro-)pores is relevant, as literature refers to the mechanical influence of the defects on the material, while smaller pores represent air pockets and material impurities, which have no significant influence on the strength of the material [34]. In Fig. 4 a magnified part shows the proportion of smaller pores that can be removed after segmentation. The segmentation of the defects is performed with the software Avizo 2020.3 (Thermo Fisher Scientific). A thresholding method is used to define a boundary within the histogram for the gray value distribution in order to binarize the 16-bit data sets into defects and material. The thresholding method used in this work is the so-called factorization method (Avizo 2020.3), which is based on the method of Otsu. In order to correct erroneously segmented areas, the data sets can be optimized with morphology-based segmentation methods in further process steps. In the context of this work, gray level dilation and erosion as described by Parvati et al. [35] have been considered. By using these methods, areas that were wrongly segmented due to artifacts can be removed. This method is particularly successful for very fine structures, such as those produced by ring artifacts, cupping or beam hardening. In literature, defects are divided into different classes with respect to their morphology, as described in the work of Hsu and Uhl [36]. With increasing porosity, pore networks and more complex geometries develop, as shown in the work of Plank et al. [37]. To describe the size of the defects, all segmented voxels of a defect are summed up and multiplied by their size to determine the volume. For the surface area of a defect, the sum of the surfaces of the voxels enclosing the defect is calculated. From these two values, further shape factors can be derived, such as the geometric deviation of the object from a sphere. The focus of the investigation is on two-dimensional defects such as delamination between CFRP layers or at the interface between aluminum and CFRP. In Fig. 4 the division of the segmented defects of a Nakajima specimen with full-circle geometry (S_{FC}) into tubular and acicular geometries as well as planar defects is shown. Therefore, the deformed specimens with the described elongation are filtered by the ratio of the eigenvalues, micro-pores and spherical defects by the shape factor and defects with a surface area below a threshold value. The filtering of the segmented defects allows various quantitative analysis, such as that of the evolution of certain shape classes, size classes or orientation classes in terms of their number versus the degree of deformation of the sample.

In this work, the defect volume and surface were used to evaluate the specimens as well as the defect rate within a region of interest. For combining the information of the Digital Image Correlation with the X-Ray datasets, a.

2D projection of the segmented data was exported, as show in Fig. 4.

3.4. Combination and correlation of results

Within this study different sensor systems have been combined. Hence, different type of data was produced. First of all, time resolved date resulted from temperature measurements, data of the testing machine (force and displacement) as well as of acoustic emission. Next, also spatially resolved data from CT-scans was recorded, whereas data from digital image correlation is time and spatially resolved. Therefore, a combination of equally resolved results is obvious. While a combination of time resolved data only requires a one-dimensional synchronization over the time axis, a local combination of data from CT and DIC is more demanding. For this purpose, an application was developed using

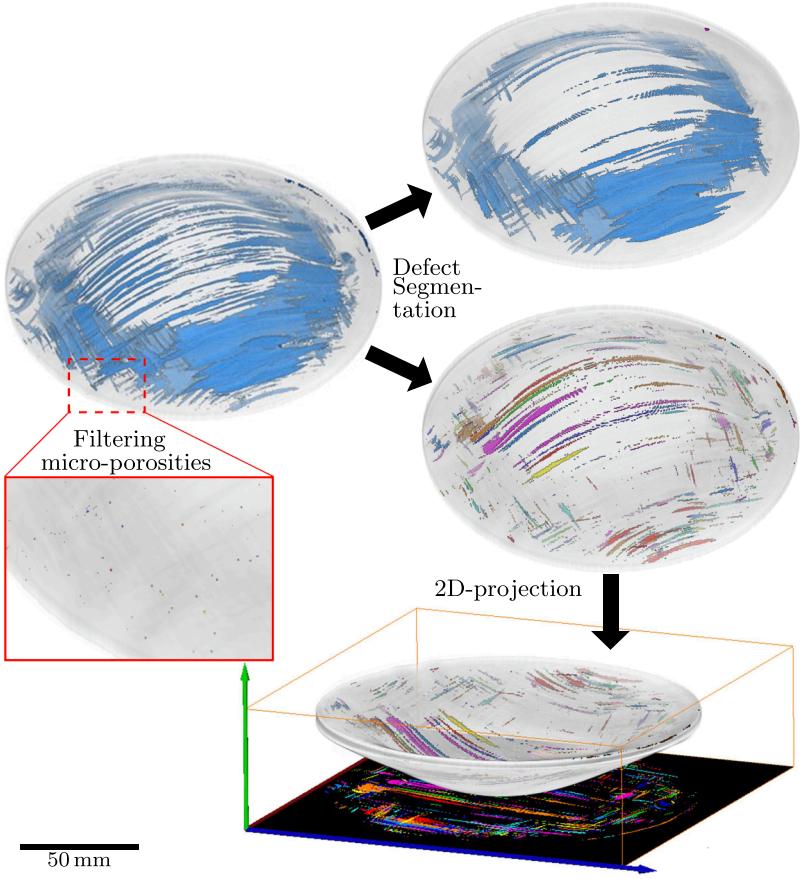

Fig. 4. Filtered mico-porosities (in red), different segmentation approaches (top right) and projection of the segmentation for data export (lower right). (For interpretation of the references to color in this figure legend, the reader is referred to the web version of this article.)

MATLAB, which was used for the processing of the DIC and CT data, as well as the local combination of these data and visualization. For easier combination and visualization 2D-projections were chosen for CT and DIC data. DIC data were transformed from subset-based data points to a pixel-based grid using interpolation. For CT and DIC data a binary mask was created, which represents the outline of the investigated sample. Using these masks and a normalized 2D cross-correlation based on differently rotated masks, the optimal position and rotation angle for the superposition of both masks was found. This allows the visualization of the superposition of segmented porosities as described earlier and different properties derived from DIC, like displacements or strains.

4. Results and discussions

Due to insufficient heating prior to the forming of the specimen, the results of the sample S_{50} are not representative and will therefore not be reported in this study.

4.1. Temperature measurements

To ensure that samples reach the required temperatures in their center as well on the surfaces, in addition to measuring the sample surface temperature during deep drawing, tests were conducted to characterize the thermal behavior of sample and tools in detail. This was realized using a thermal camera for inspection of the sample's bottom surface temperature distribution (see Fig. 5), as well as several thermocouples of type K on relevant locations of the tool and on the sample bottom and top, as well as inside the sample right at the sample center. In this case the sample top surface is the one being contacted by the punch and the bottom is the one faced by the DIC cameras. The thermal imaging data show a uniform temperature distribution in the relevant center region of all sample types with an increase in temperature closer to the edges, where they are in contact with the actively heated tooling.

The comparison between the temperature tests conducted with samples of different shapes shows a dependency of heating rate and maximum possible temperature with sample size, as show in Fig. 6. Therefore, this information was later used for the samples, where not direct temperature measurement at the sample center was possible. The observed temperature offset could then be used to estimate if the required sample temperature was reached, without placing a thermocouple in the sample center. It is obvious, that all samples can reach the required temperature, but take very different amounts of time. While samples with larger surfaces, like S_{FC} and S_{90}, take only around 60 min to reach 220 °C, narrower samples take up to 120 min. This is probably caused by a combination of different amounts of contact area to the heated tool and convection effects in the temperature chamber.

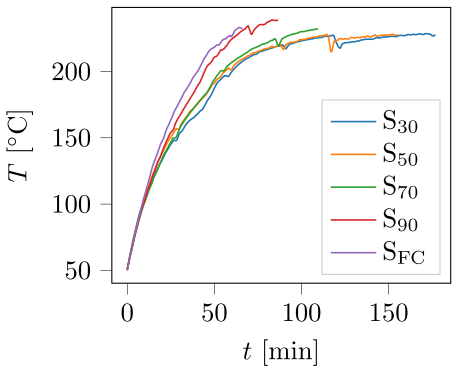

Fig. 6. Temperature at the center of the upper sample surface for different sample geome- tries during heating from room temperature.

4.2. Digital image correlation

The DIC data obtained in the experiments were used to perform a quantitative analysis of the load condition, as well as qualitative observations of effects, visible in the displacement and strain fields. For the load condition analysis, a similar approach to the classical forming limit curve was chosen. In contrast, not only the point right before fracture was evaluated, but for several steps of deep drawing major (ε_1) and minor strains (ε_2) – as defined and applied by the test standard [31] – were evaluated in a representative circular region of interest at the center of the sample. As the deep drawing of the hybrid specimens was conducted in steps of 5 mm, the strain values for each step were added up to result in a cumulative strain curve. By performing the same procedure on the verification dataset from the tests on monolithic aluminum, the influence of the hybridization of the material system can be seen. According to the standard ISO 12004–2 [31] a forming limit diagram (FLC) is a diagram containing major/minor strain points and can distinguish between safe points and necked or failed points according to a distinct loading that is achieved by sample design. paths in a

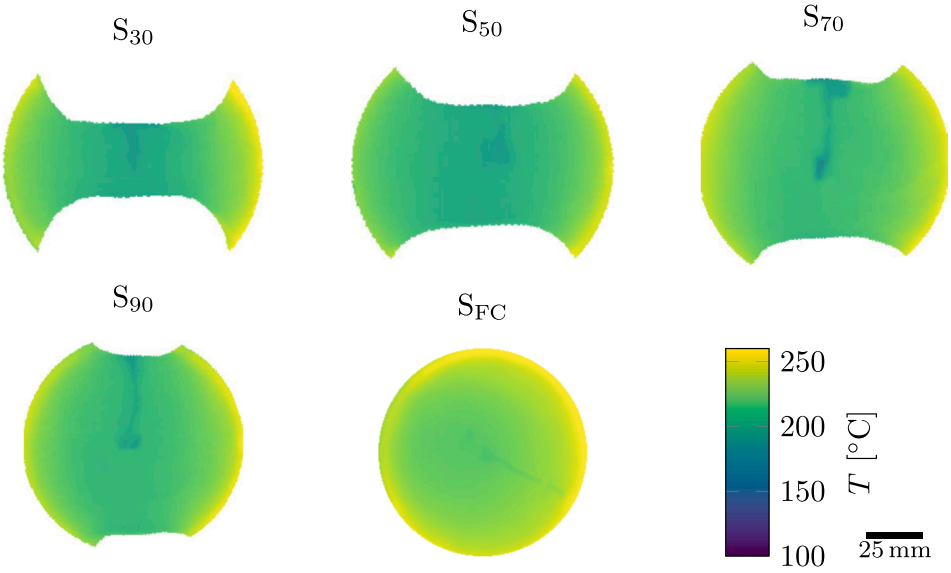

Fig. 5. Thermal images of the exposed, lower surface of all sample types after a sufficient period. Especially the relevant middle section of the samples shows a homogeneous tempera- ture distribution. Visible artifacts are due to applied thermocouples on the surface.

diagram of major and minor strains. The transition from safe to failed points is defined by the forming-limit curve (FLC). For comparison, Fig. 7a shows the forming limit curve (FLC) (black, dashed line) for the monolithic Al 1050A samples at comparable temperatures to the forming of the hybrid specimens, as well as the trajectory for each sample up to the failure point in color, while Fig. 7b only represents the resulting trajectories for the hybrid FML samples. In general, it can be noted, that apart from the full-circle sample, the strains experienced by the monolithic metallic samples (in detail ε_1) are higher. It seems, that especially for these sample geometries, where not the full circumference of the sample is clamped, the more complex sample cross-section leads to different load distributions, while the deformation in the form of the ratio of $\frac{\varepsilon_1}{\varepsilon_2}$ on the observed surface is similar. However internal stress distribution and/or edge effects might be responsible for the premature failure of the samples. In more detail, it might be possible that pure aluminum shows higher damage tolerance under multi-axial loading compared to the hybrid fiber-metal laminate and the fiber-reinforced component in the hybrid FML – due to the inherent anisotropy – failed at lower strains. Hence, this internal damage possibly weakened the surrounding aluminum, so that external cracks appeared earlier. For both metal and FML samples the occurrence of cracks in the metal were used as the termination criterion. This did not proof to be suitable for the FML samples, as cracks did not occur in the center region, as required by the test standard, but rather off center or close to the clamping area. Therefore, a comparable displacement and sample geometry leads to different strains experienced by the outer metal layer compared to the monolithic metal sample, probably due to the stress distribution along the more complex material cross-section. To return to the question of what a suitable termination criterion for hybrid FML can look like to evaluate the formability and a form limiting curve, it is clear that a criterion based on external cracks is not useful for hybrid fiber-metal laminates and must be adapted accordingly, since failure occurring inside of the hybrid material significantly reduces formability. Additionally, other types of failure in the polymer layer of the FML cannot easily be considered in-situ and therefore not be used as a termination criterion. One advantage of using 3D digital image correlation is the possibility to perform qualitative observations on all kind of data, evaluated from the recorded displacement fields. Especially areas with higher or lower than average strain can be of special interest. This can be observed for example in Fig. 8, where an area of center shows strains up to 2 % higher than the average on the sample surface (area marked by red dashed line). Also, the area near the straight edges shows a major strain close to zero (area marked by red dotted line). These two signatures could be related to internal effects, such as i.e. delamination and are the main motivation for the ex-situ X-Ray CT measurements.

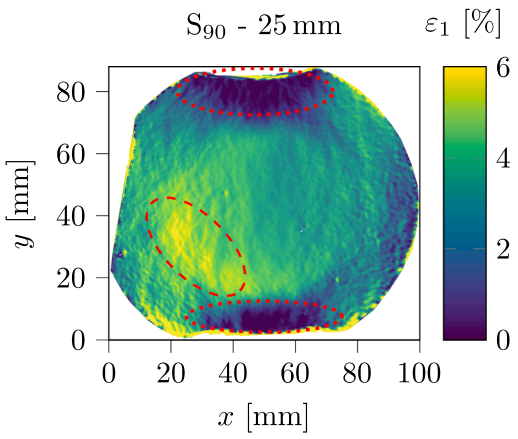

Fig. 8. 2D-projection of the major strain field of sample S_{90} width after 25 mm of deep draw- ing.

4.3. Acoustic emission analysis

Using acoustic emission analysis for the described process was a new approach. It was observed that the method used to actively cool the sample after deep drawing heavily influences the quality of the acoustic emission data recorded. While using a flow of compressed air produced a very high level of noise, the application of compact air fans (as shown in Fig. 2) at the bottom of the sample holder showed much better results, both concerning the cooling rate and noise level in the acoustic emission data.

For all stages of the deep drawing, acoustic emission signals obtained by all three sensors were recorded, but only evaluated after reaching the maximum force, as the focus was to find signatures from effects that happened during the cooling of the material. One reason is, that the sample is not expected to emit sound before and during deep drawing, as the polymer is in a molten state and therefore it is unlikely that acoustic emission signals are generated. Also, unwanted signals can occur during the deep drawing process itself. The signal first underwent a Δt-Filter of 100 µs to eliminate most signals, not originating from the area of the sample. This was validated previously using the identical sensor setup with a mounted sample while performing PLB-tests on all relevant surfaces of the test setup. With the chosen time and the geometry of the test setup, only acoustic signals originating from the vicinity of the sample itself were recorded. After a general feature extraction on all acoustic events an additional energy filter with an empirical value of 0.01 nJ was applied to only consider relevant signals. Fig. 9 shows the progression of

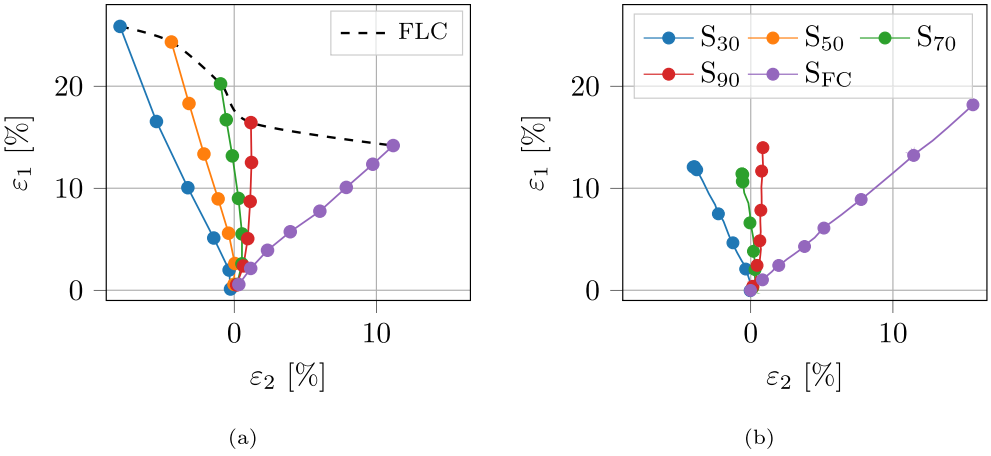

Fig. 7. Forming limit diagram (FLD) for monolithic aluminum (a) and hybrid samples (b). For the Al-samples one representative sample with valid failure for each sample geometry was chosen, for the FML samples only one sample for each geometry was tested. In (a) the dashed line indicates the forming limit curve (FLC), hence transition from safe points for forming to failure. In (b) only the trajectories are shown.

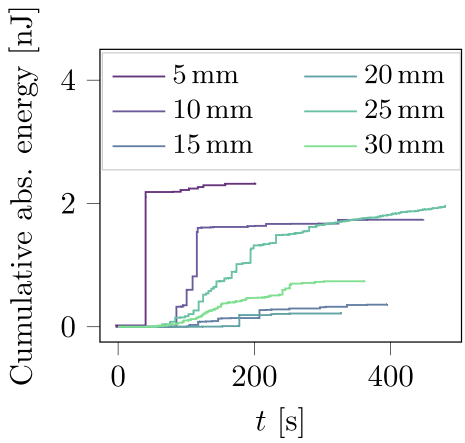

Fig. 9. Recorded cumulative absolute energy from acoustic emission during cooling of sample S_{90} for all deep drawing steps from 5 mm to 30 mm.

the cumulative absolute energy of detected acoustic events over time for each deep drawing step from 5 mm to 30 mm. $t = 0$ is defined as time of maximum force, therefore cooling of the sample started a few seconds later. The highest acoustic activity can be observed between 30 s and 200 s after the cooling initiation (see Fig. 13, where cooling onset is marked), in which time-frame the main cooling of the sample occurs Secondly, the first steps with the least amount of deep drawing show the highest amount of total energy measured. At later stages the total energy decreases significantly. This is probably due to the low consolidation pressure, while the round die comes into contact with the flat sample. Therefore, more deconsolidation can occur. This will be further supported in section 4.4 by CT measurements.

4.4. X-ray computed tomography

After successful segmentation of the samples over the entire sample area, so-called regions of interest (ROI) were created to evaluate the area of the respective sample that is permitted for evaluation in the DIN EN ISO 12004–2 standard. The area was extended to 30 mm around the top pole to use the same section as in the application of the cut line method. This evaluation was carried out for the specimens S_{30}, S_{70}, S_{90} and S_{FC} at all forming stages. Subsequently, the proportion of air inclusions in the drawn material section was determined. The results of this evaluation are plotted in Fig. 10. The curves of the air content over the degree of deformation of S_{70} and S_{FC} differ significantly in this evaluation from the curves of S_{30} and S_{90}. As can be seen in Fig. 12, in different parts of the sample larger areas show either general delamination or detachment of the inner aluminum layer. It is assumed that this is due to a combination of the before mentioned low consolidation pressure in the beginning and the mismatch in the thermal expansion coefficient between the CFRP and the aluminum layer. While the PA-6 matrix solidifies at

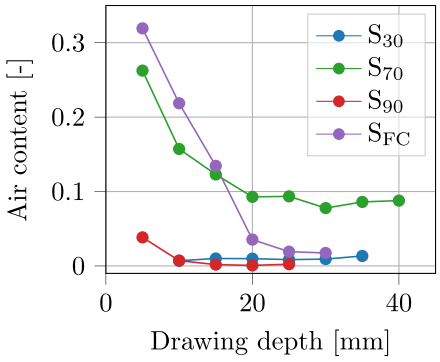

Fig. 10. Defect rate over drawing depth for all samples.

temperatures below 220 °C, stresses build up in the aluminum during the further cooling process, leading to partial detachment in the case of the S_{FC} and S_{70} specimens. In general, the specimens have in common that the air content decreases with increasing degree of deformation, which can be attributed to the before mentioned partly low consolidation pressure in areas not yet in contact with the punch. In the S_{30}, S_{70} and S_{90} specimens, there is a slight increase in the air content at final failure. Reaching a minimum air content could thus be used as an indicator of imminent failure of the specimen. In addition to air content in the samples, the total surface area and volume of the defects was analyzed, as shown in Figs. 10 and 11b for sample S_{70}. This shows, that with increased amount of deep drawing the amount of very small defects is decreased, while medium-sized defects first become more common until drawing depths of around 15 mm before decreasing and combining to form fewer but larger defects. Having a closer look at reconstructed slices of the CT-measurements (see Fig. 12, as well as the quantitative evaluation of defect area and volume (see Figs. 10 and 11 deconsolodation becomes visible. Initially only a small part of the punch is in contact with the sample and thus large parts of the sample are unsupported and experience delamination and the creation of voids. This improves with further deep drawing, until the whole non-clamped part of the sample is contacted by the punch.

4.5. Fusion of sensor data

Using different sensors and data acquisition systems gives the opportunity to combine the recorded and evaluated data of all time dependent systems. In this case data from the universal testing machine (force and displacement), acoustic emission analysis (cumulative absolute energy) and thermocouples were combined. Synchronization of data from the universal testing machine and the acoustic emission system was accomplished by the point of maximum force, as force data were also recorded in the acoustic emission system via an analog in-put. Temperature data were then synchronized by hand using the temperature change on contact with the punch at the beginning of the deep drawing procedure. A combined graph of all these data gives a good overview over the whole process (see Fig. 13). At the beginning, when the punch contacts the sample and moves the distance of 5 mm, the measured force first increases quickly until the punch reaches its end position. At that moment the force starts to decrease due to slower deforming mechanisms inside the sample, mainly the molten polymer. Also, the sample temperature shows a slight increase after contact with the punch, which shows that initially the higher temperature tool prevents a sudden cooling of the sample. Especially interesting here is the time at which most high energetic acoustic emission events happen in combination with the temperature change of the sample after contact with the punch. The active cooling of the sample starts at around 100 s, at which point a decrease in the temperatures, as well as the start of the detection of acoustic emission signals can be observed. The cumulative amount of measured acoustic energy shows a stepwise increase over the next few minutes, with steps sizes varying from pJ to several tenths of nJ. This indicates the formation of differently sized defects inside the sample, which occur due to the change in temperature and thus thermal stresses between the different materials involved. To ensure that the observed increase in AE signals can be attributed to effects inside the sample- in addition to using the Δt-Filter – additional measurements were conducted without the sample and with metallic samples to create a baseline of acoustic noise present during the measurement. With this information it was possible to remove unwanted signals – if present – either using gates or filters on the hardware side or in post-processing.

4.6. Correlation of DIC and CT results

As the results from the digital image correlation are resolved both locally and time resolved, they bridge the gap between time resolved data as discussed before and locally resolved data from the CT scans. In

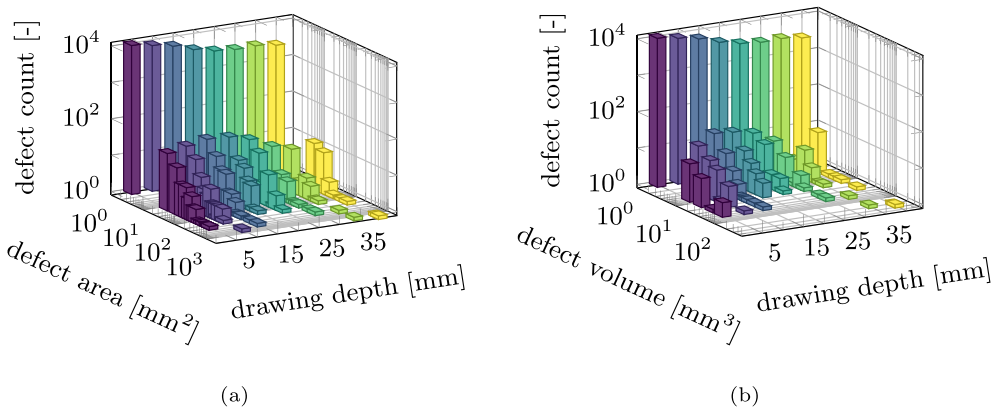

Fig. 11. Distribution of defect area (a) and volume (b) over drawing depth for sample S_{70}.

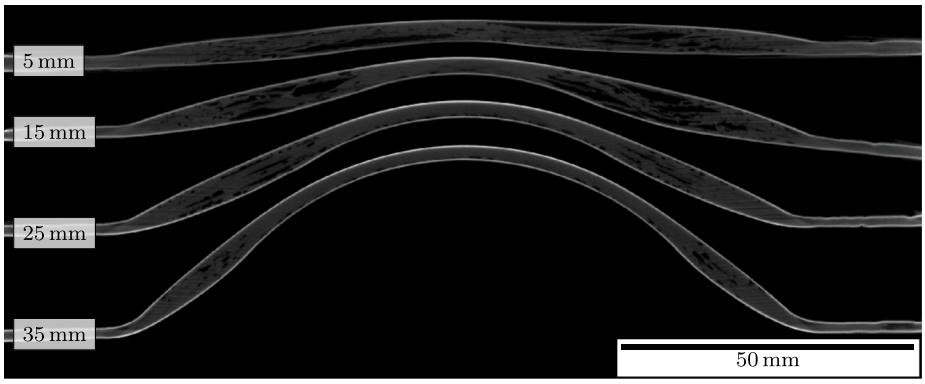

Fig. 12. CT-slices of the sample S_{FC} after four different stages of deep drawing (5 mm, 15 mm, 25 mm and 35 mm.

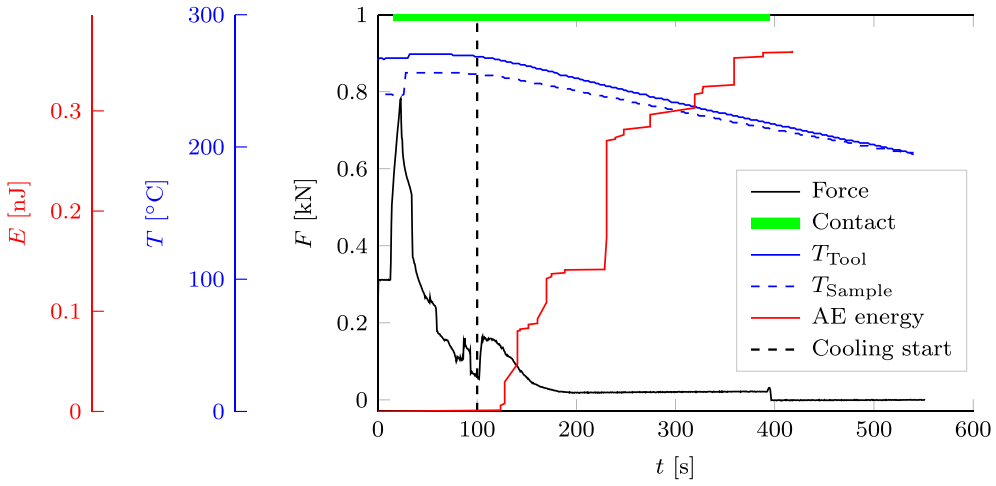

Fig. 13. Time based fusion of sensor data from the testing machine, temperature measurements and acoustic emission analysis.

this the projections of preselected porosity from CT and different strain and displacement fields from DIC were combined. As an example, Fig. 14 shows the strain field in *x*-direction (for information of coordinate system see Fig. 1a) from the DIC data as an overlay over relevant porosity extracted from the CT data. In this case the narrow part of the sample shows higher strain than average, whereas regions closer to clamping show only slightly positive strain values. The main amount of porosity occurs in the region of highest strain gradient, in this case in the vertical region between the radii of the sample geometry (red, dotted areas in Fig. 14). Further it can be observed that in these regions of high strain gradient the main orientation of porosities is also in the *x*-direction, whereas in region with more constant strain distribution (in the center and closer to the horizontal edges) the fewer porosities are more oriented along the *y*-axis (red, dashed areas in Fig. 14).

5. Conclusion

A new method was developed to investigate the formability of thermoplastic Fiber Metal Laminates (FML), based on an adaption of the Nakajima-test, that is normally considered for monolithic metallic materials. Therefore, a lab-scale setup was created, using special tooling and a universal testing machine. For better understanding of the failure

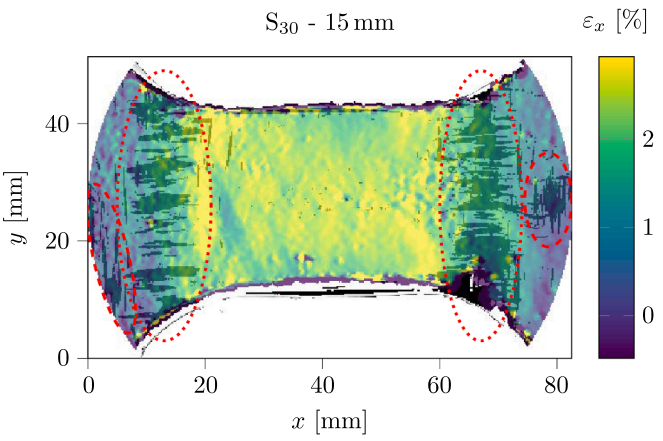

Fig. 14. Superposition of CT and DIC data for sample S_{30} after 15 mm of deep drawing. Shown is strain field in *x*-direction ϵx in color and relevant porosity in black.

process, a combination of in- and ex-situ monitoring was chosen. During stepwise deep drawing, 3D digital image correlation, acoustic emission analysis, temperature measurements as well as force and displacement data from the testing machine were captured. In between the deep drawing steps the sample was cooled and CT scans were performed. Coming back to the main research questions, the proposed methodology is able to combine different in- and ex-situ measurement techniques in a heated environment and with the proposed synchronization of data, valuable information of failure evolution and forming limits of hybrid fiber-metal laminates can be derived. In more detail, capturing of the evolving strain fields can – in combination with CT-images – be especially to evolving delamination. In addition, acoustic emission helps to"hear" failure in the inside of the material that might not be visible at the surface. However, although the information gathered during these tests as well as the new insights from combining different measurement and monitoring systems is promising, it has to be recognized, that only a limited number of specimens haven been evaluated. Nevertheless, the presented approach is a valuable first step to gain a more profound understanding of forming abilities of fiber metal laminates especially in comparison to structures made from pure aluminum. To sum up investigations of forming behavior of fiber-metal laminates, the forming limit curve that is a material parameter reflecting of the limiting strains resulting in necking failure as a function of strain path, is not a suitable way to define forming limits for hybrid materials as failure is very complex and not always visible from the outside. Hence more complex criteria also considering internal failure have to be defined in future. The combination of in- and ex-situ monitoring methods shows that connections can be made between internal defects, like delamination or porosities, and external measurement data, like strain anomalies or AE events. Such connections could in future be used to create additional termination criteria that allow more suitable and more conservative estimations for the formability of thermoplastic FML. Taking this in mind, a consequent step would be to extract all necessary information purely from in-situ measurement techniques (DIC and AE) in order to avoid the expansion of the test specimen, or to implement the entire setup (testing machine and measurement techniques) in a radiation-proofed room to carry out robot-based computed tomography.

CRediT authorship contribution statement

Florian Thum: Writing – original draft, Visualization, Methodology, Investigation, Conceptualization. **Marco Korkisch:** Writing – review & editing, Writing – original draft, Visualization, Validation, Software, Methodology, Investigation, Formal analysis, Data curation, Conceptualization. **Anna Trauth:** Writing – original draft, Supervision, Project administration, Conceptualization. **Markus G.R. Sause:** Writing – review & editing, Supervision, Funding acquisition, Conceptualization.

Declaration of competing interest

The authors declare that they have no known competing financial interests or personal relationships that could have appeared to influence the work reported in this paper.

Acknowledgements

This research was conducted in the course of the publicly funded projects MAI CC4 HybCar and MAI CC4 hybrid, funded by the Bavarian Ministry of Economic Affairs, Regional Development and Energy (former: Bavarian Ministry of Economic Affairs and Media, Energy and Technology).

Data availability

Data will be made available on request.

References

[1] Vlot A, Gunnink JW. Fibre metal laminates: an introduction, Springer eBook Collection, Springer Netherlands, Dordrecht; 2001. doi:10.1007/ 978-94-010-0995-9.
[2] Fleischer J, Nieschlag J. Introduction to CFRP-metal hybrids for lightweight structures. Prod Eng 2018;12:109–11. https://doi.org/10.1007/s11740-018-0825-0.
[3] Vogelesang LB, Meyers LG, van Velze TM. Laminate of metal sheets and continuous filaments-reinforced thermoplastic synthetic material, as well as a process for the manufacture of such a laminate; 1991.
[4] Krishnakumar S. Fiber metal laminates - the synthesis of metals and composites. Mater Manuf Process 1994;9:295–354. https://doi.org/10.1080/10426919408934905.
[5] Reyes G, Kang H. Mechanical behavior of lightweight thermoplastic fiber–metal laminates. J Mater Process Technol 2007;186:284–90. https://doi.org/10.1016/j.jmatprotec.2006.12.050.
[6] Carrillo J, Cantwell W. Mechanical properties of a novel fiber–metal laminate based on a polypropylene composite. Mech Mater 2009;41:828–38. https://doi.org/10.1016/j.mechmat.2009.03.002.
[7] Van Hoa S, Duc Hoang M, Simpson J. Manufacturing procedure to make flat thermoplastic composite laminates by automated fibre placement and their mechanical properties. J Thermoplast Compos Mater 2017;30:1693–712. https://doi.org/10.1177/0892705716662516.
[8] Nestler D, Trautmann M, Zopp C, Tröltzsch J, Osiecki T, Nendel S, et al. Continuous film stacking and thermoforming process for hybrid CFRP/aluminum Laminates. Proc CIRP 2017;66: 107–112. doi:10.1016/j.procir.2017.03.221.
[9] K. Lange (Ed.), Umformtechnik Handbuch für Industrie und Wissenschaft, Springer Berlin Heidelberg, Berlin, Heidelberg, 1988.
[10] A. Kuppert, Erweiterung und Verbesserung von Versuchs- und Auswertetechniken für die Bestimmung von Grenzformanderungskurven, Ph.D. thesis, Meisenbach, Bamberg, 2019.
[11] DIN Deutsches Institut für Normung e.V., DIN EN ISO 12004-2:2009-02, Metallische Werkstoffe - Bleche und Bänder - Bestimmung der Grenzformänderungskurve-Teil 2: Bestimmung von Grenzformänderungskurven im Labor, Technical Re- port, Beuth Verlag GmbH, Berlin, 2008.
[12] Merklein M. Charakterisierung von Blechwerkstoffen für den Leichtbau. Bamberg: Meisen- bach; 2006.
[13] Joshi AR, Kothari KD, Jhala DRL. Effects of different parameters on deep drawing process: review. International Journal of Engineering Research & Technology 2013;2. https://doi.org/10.17577/IJERTV2IS3393.
[14] Lecompte D, Smits A, Bossuyt S, Sol H, Vantomme J, Van Hemelrijck D, et al. Quality assessment of speckle patterns for digital image corre- lation. Opt Lasers Eng 2006;44:1132–45. https://doi.org/10.1016/j. optlaseng.2005.10.004.
[15] M. G. Sause, In Situ Monitoring of Fiber-Reinforced Composites, volume 242 of *Springer Series in Materials Science*, Springer International Publishing, Cham, 2016. doi:10.1007/978-3-319-30954-5.
[16] B. D. Carleer, Finite element analysis of deep drawing, Ph.D. thesis, University of Twente, 1997. doi:10.3990/1.9789090103587.
[17] T. Atul S, M. C. L. Babu, A review on effect of thinning, wrinkling and spring- back on deep drawing process, Proceedings of the Institution of Mechanical Engineers, Part B: Journal of Engineering Manufacture 233 (2019) 1011–1036. doi:10.1177/0954405417752509.
[18] Hiroi T, Nishimura H. The influence of surface defects on the forming-limit diagram of sheet metal. J Mater Process Technol 1997;72:102–9.
[19] P. E. Smith, D. Lee, Determination of Forming Limits for Aluminum Alloys, in: SAE Technical Paper Series, SAE Technical Paper Series, SAE International400 Commonwealth Drive, Warrendale, PA, United States, 1998.

[20] Tasan CC, Hoefnagels JPM, Dekkers ECA, Geers MGD. Multi- Axial Deformation Setup for Microscopic Testing of Sheet Metal to Fracture. Exp Mech 2012;52: 669–78.
[21] J. Pavan Kumar, R. Uday Kumar, B. Ramakrishna, B. Ramu, K. Baba Saheb, Formability of sheet metals – A review, IOP Conference Series: Materials Science and Engineering 455 (2018) 012081. doi:10.1088/1757-899X/455/1/012081.
[22] Gottstein G. Materialwissenschaft und Werkstofftechnik. Springer Vieweg, Berlin: Springer-Lehrbuch; 2014.
[23] J. J. Burke, V. Weiss (Eds.), Advances in Deformation Processing, Springer US, Boston, MA, 1978.
[24] Tonshoff HK, Bunte J, Meier O, Engelbrecht L. Deformation Behaviour of Sheet Metals in Laser Assisted Hydroforming Processes. Sheet Metal 2005;2005:361–8.
[25] Hsu E, Carsley JE, Verma R. Development of forming limit diagrams of aluminum and magnesium sheet alloys at elevated temperatures. J Mater Eng Perform 2008; 17:288–96.
[26] Y. Dahan, Y. Chastel, P. Duroux, J. Wilsius, P. Hein, Procedure for the experimental determination of a forming limit curve for Usibor 1500 P, Gÿor; 2007.
[27] Bariani PF, Bruschi S, Ghiotti A, Turetta A. Testing formability in the hot stamping of HSS. CIRP Ann 2008;57:265–8.
[28] Turetta A. Investigation on thermal, mechanical and microstructural properties of quenchenable high strenght steels in hot stamping operations. Padova: University of Padova; 2008. Ph.D. thesis.
[29] Merklein M, Kuppert A, Geiger M. Time dependent determination of forming limit diagrams. CIRP Ann 2010;59:295–8.
[30] ALUJET GmbH, Technical Datasheet – Aluminiumfoil; 2021.
[31] DIN Deutsches Institut für Normung e.V., DIN EN ISO 12004-2:2009-02, Metallische Werkstoffe - Bleche und Bänder - Bestimmung der Grenzformänderungskurve- Teil 2: Bestimmung von Grenzformänderungskurven im Labor, Technical Report, Beuth Verlag GmbH, Berlin, 2009.
[32] DGZfP, DGZfP-SE 02:2014-07 - Verifizierung von Schallemissionssensoren und ihrer Ankopplung im Labor, Technical Report, DGZfP, Berlin, 2014.
[33] D. Kiefel, Quantitative Porositätscharakterisierung von CFK-Werkstoffen mit der Mikro-Computertomografie, Ph.D. thesis, TU München, München, 2017.
[34] E. A. Birt, R. A. Smith, A review of NDE methods for porosity measurement in fibre-reinforced polymer composites, volume 46, Farnborough; 2004.
[35] Parvati K, Prakasa Rao BS, Mariya Das M. Image Segmentation Using Gray- Scale Morphology and Marker-Controlled Watershed Transformation. Discret Dyn Nat Soc 2008:1–8.
[36] Hsu DK, Uhl KM (Eds.), A morphological study of porosity defects in graphite-epoxy composites, Springer, Boston; 1987.
[37] Plank B, Mayr G, Reh A, Kiefel D, Kastner J. Evaluation and visualisation of shape factors in dependence of the void content within CFRP by Means of X-ray computed tomography, Prag; 2014.